Chapter 7

Synthesis of metal based nanomaterials

In this chapter, synthesis of metal based nanomaterials by calcination and roasting of plant based precursors were discussed. A total of four plant based precursors (plant charcoal, waste bond paper, sisoo leaves, and krishnachura or gulmohar leaves) were used for the synthesis of metal based nanoparticles. Antimicrobial efficacy, electrochemical behaviour, photocatalytic activity, of the synthesised materials was investigated.

7.1. Introduction

Besides carbon nanomaterials, metal based nanomaterials have also attracted great interest from both fundamental as well as applied research point of view owing to their interesting physical and chemical properties and also promising applications in many fields including catalysis, coatings, membranes and electronics [1, 2]. Among the numerous metal based nano-sized materials synthesized during the past decade, calcium carbonate and calcium sulphate received much attention due to their wide applications in the areas of polymers, paints, plastics, rubber, filler etc [3-5]. It is reported that $CaCO_3$ nano-particles acted as additives in lubricating oils and exhibited good load-carrying capacity, antiwear and friction-reducing properties [6]. Calcium carbonate ($CaCO_3$), a typical biomineral, is known to occur in both living organisms

and nature possessing biological activities of protein-adhesion properties, cell compatibility, and hard tissue compatibility [7, 8]. The mineral occurs in four polymorphs: calcite, vaterite, aragonite and amorphous calcium carbonate. Owing to enhanced thermodynamic stability, calcite polymorph is considered as most important phase in industrial applications such as in ceramics, cosmetics, pigments, rubber industry etc [9, 10]. The material is used as drug-support with hydrocortisone phosphate [11-13]. The high porosity and surface area coupled with low mass transport barrier of $CaCO_3$ particles make them suitable for biosensors and other environmental applications [14, 15]. The mineral is also used as a filler material in paper to improve ink retention, brightness and water resistance [16]. Calcium sulphate being more biocompatible as compared to calcium phosphate, is a viable bone graft substitute material for ridge augmentation, bone defect filler, sinus augmentation and guided tissue regeneration [17- 19]. Calcium sulphate is used for drug delivery because of its degradation properties [4, 19-22]. Nanosized $CaSO_4$ in an inject-able form reduces surgical invasiveness, good mold-ability, fill deep spaces and ability to adapt to a defect area and thereby promoting cell migration from the healthy surrounding tissues [23]. There are extensive reports on chemical synthesis of $CaCO_3$ and $CaSO_4$ nanoparticles [23-25], however, bio inspired waste derived synthetic routes are scant. For the preparation of nanomaterials from carbonaceous sources subjecting the starting material to high temperatures has been a common approach. The vapourised material, which is rich in materials in the nano domain, is condensed and collected. Most often, not much attention is paid to the leftover solid residue. As a sequel to the ongoing program of utilising waste materials and renewable plant based resources for obtaining nanoparticles, we were motivated to study that nonvolatile leftover solid residue from calcination or roasting. Accordingly, we report in this chapter inexpensive, renewable and scalable green protocol for the synthesis of calcium sulphate and calcium carbonate nanoparticles from variety of plant based sources.

7.2. Calcium sulphate nanocomposites from plant charcoal

7.2.1. Materials

Commercially available plant charcoal was used the synthesis of calcium sulphate nanocomposite. Charcoal is usually made by charring wood in the absence of air.

7.2.2. Synthesis of calcium sulphate nanocomposite

A block of plant charcoal (approx. 1.5 g), finely crushed into powder, was heated over a Bunsen burner flame to red hot for two hours. Carbon and other volatile oxidisable materials were removed under these conditions. A white powder residue remained after heat treatment, which was analyzed 'as obtained'. The yield recorded was 2.8 g, (~30%).

7.2.3. Results and discussion

The calcium sulphate nanocomposite has been accessed from plant charcoal by roasting in a Bunsen burner. The yield of the synthesized materials was found to be around 30% by weight of initial mass. In normal wood ash, the major component is calcium carbonate. Mishra and co-workers reported a very good account of wood ash composition as the function of furnace temperature [26]. They reported the presence of $CaCO_3$, $K_2Ca(CO_3)_2$, $K_2Ca_2(SO_4)_3$ at 600^0C and CaO, MgO and Ca_2SiO at $1{,}300^0$C [26].

7.2.3.1. Scanning electron microscopy of calcium sulphate nanocomposite

The SEM images showed the presence of spherical nano-scaled domains forming micro-scale aggregates (**Fig.7.1**). The size of the spherical particle has been evaluated to be ~600 nm.

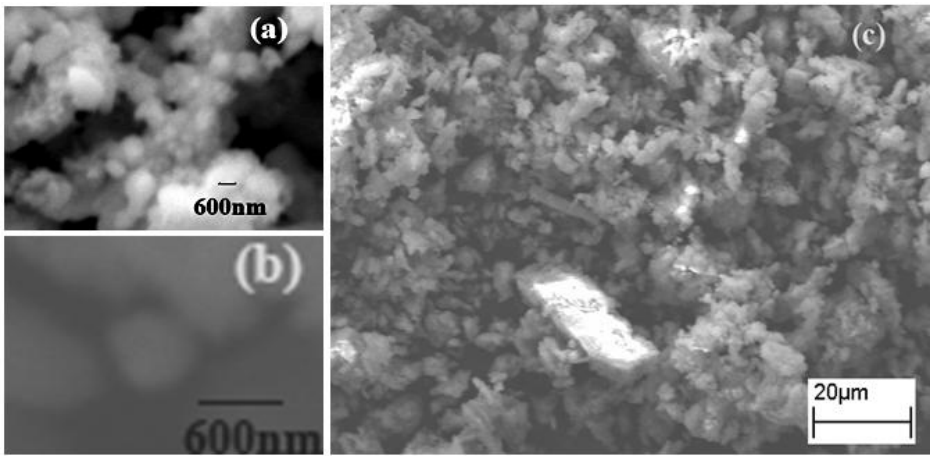

Fig.7.1. (a) SEM image of the synthesized material**, (b)** single particles**, (c)** lower resolution image showing aggregates of particles

7.2.3.2. Energy dispersive spectral (EDS) study

Energy dispersion spectroscopy **(Fig.7.2)** was performed to analyse the elemental composition. The study revealed the presence of oxygen, sulphur and calcium as the major constituents, along with minor contributions from sodium, magnesium, aluminium, silicon, chlorine, potassium and iron **(Table 7.1)**.

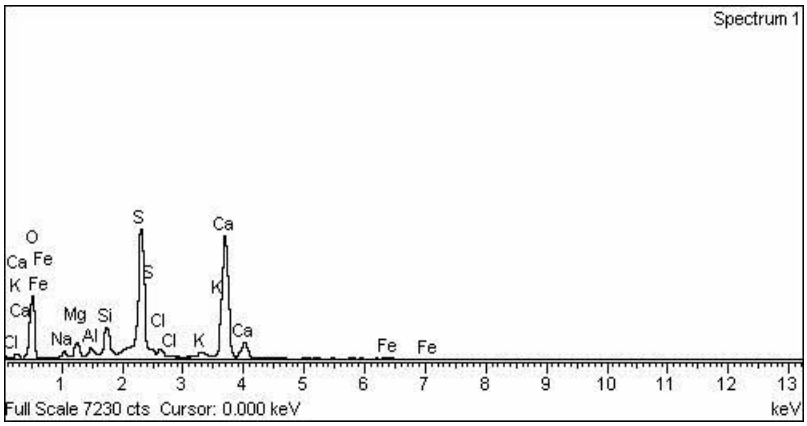

Fig.7.2. EDS of the calcium sulphate nanocomposite

Table 7.1 Elemental composition of the nanocomposite

Element	App Conc.	Intensity	Weight%	Weight% Sigma	Atomic%
O	37.55	0.4370	49.94	0.78	68.23
Na	1.55	0.6542	1.38	0.18	1.31
Mg	2.30	0.6318	2.12	0.15	1.90
Al	1.13	0.7350	0.89	0.11	0.72
Si	4.65	0.8396	3.22	0.15	2.50
S	25.86	0.9334	16.10	0.34	10.97
Cl	1.49	0.7180	1.21	0.12	0.75
K	1.27	1.0228	0.72	0.10	0.40
Ca	39.14	0.9582	23.74	0.43	12.94
Fe	0.95	0.8093	0.68	0.15	0.27
Total			100.00		

7.2.3.3. X-ray diffraction studies

The X-Ray diffraction (XRD) spectrum of the material is presented in **Fig.7.3**. The XRD pattern (and the data from EDS study) of the sample indicated the material to be

mainly the $CaSO_4$ phase. The EDS study indicated the atomic ratio of calcium and sulphur to be approximately 1:1, along with a high percentage of oxygen. The structure was tried to be resolved from the powder pattern using WinGX suit [27]. The pattern was found to show high similarity with the powder pattern simulated from the single crystal data of $CaSO_4$ with space group A m m a [28,29] using Mercury 1.4.1 suit [30]. Both the peak position and the intensity ratio exhibited a close match. The experimental (with corresponding Miller Indices) and the simulated patterns are presented in **Fig.7.3** for comparison. The presence of the $CaSO_4$ phase also explains the high percentage of oxygen. The rest amount of oxygen seems to arise from other minor metal oxides, which are responsible for the minor extra reflections in the pattern (the unindexed reflections at 27^0 and at 39.5^0). No detectable evidence for the presence of CaO was found in the XRD pattern of the sample.

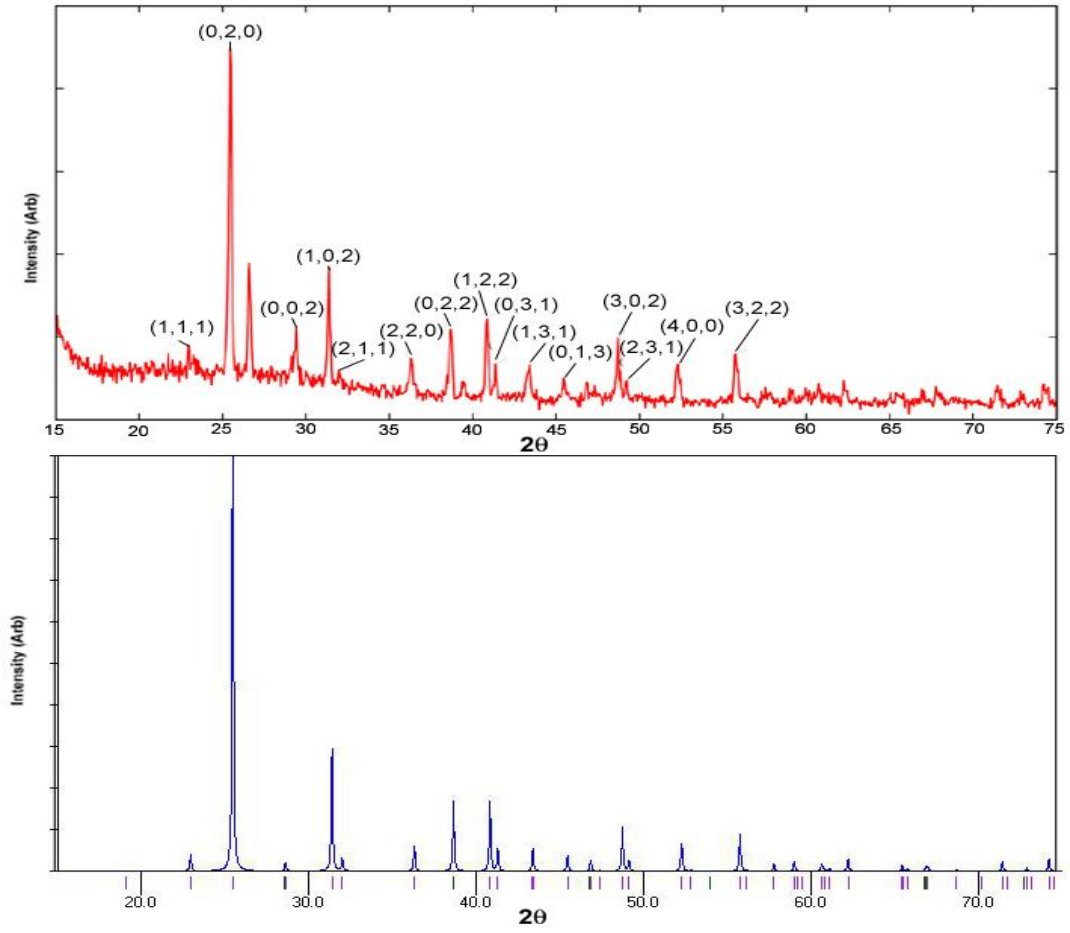

Fig.7.3. Powder X-ray diffraction pattern of the material. At the top the experimental (red) and the bottom the simulated powder pattern (blue) for $CaSO_4$ are plotted.

7.2.3.4. Study of antimicrobial activity

The activity of the material against different microorganisms was monitored with the as prepared sample. Disc diffusion method was used to determine the zone of inhibition. The material exhibited a very good inhibitory effect against *Streptococcus faecalis* and *Bacillus subtilis* and lesser activity against *Klebsilla pneumonae, E. coli, Proteus vulgaris* and *Pseudomonas aeruginosa* relative to standards ciprofloxacin and clotrimazole **(Table7.2).** The solvent chloroform has no antimicrobial activity as such. The antimicrobial property of the material seems to arise due to changes in the microenvironment in the vicinity of organism-particle contact area causing damage to the cell membranes on intimate contact between the cell and particle [31].

Table7.2. Antimicrobial activity of the as obtained material

Sl. No.	Microbes	Standard (Zone of inhibition)	Solvent	Nanocomposite (Zone of inhibition)
1	*Streptococcus faecaelis*	40 mm	Nil	18 mm
2	*Bacillus subtilis*	32 mm	Nil	20 mm
3	*Klebsilla pneumoni*	30 mm	Nil	12 mm
4	*E. coli*	35 mm	Nil	13 mm
5	*Proteus vulgaris*	40 mm	Nil	12 mm
6	*Pseudomonas aeruginosa*	30 mm	Nil	12 mm

The standard used are clotrimazole and ciprofloxacin

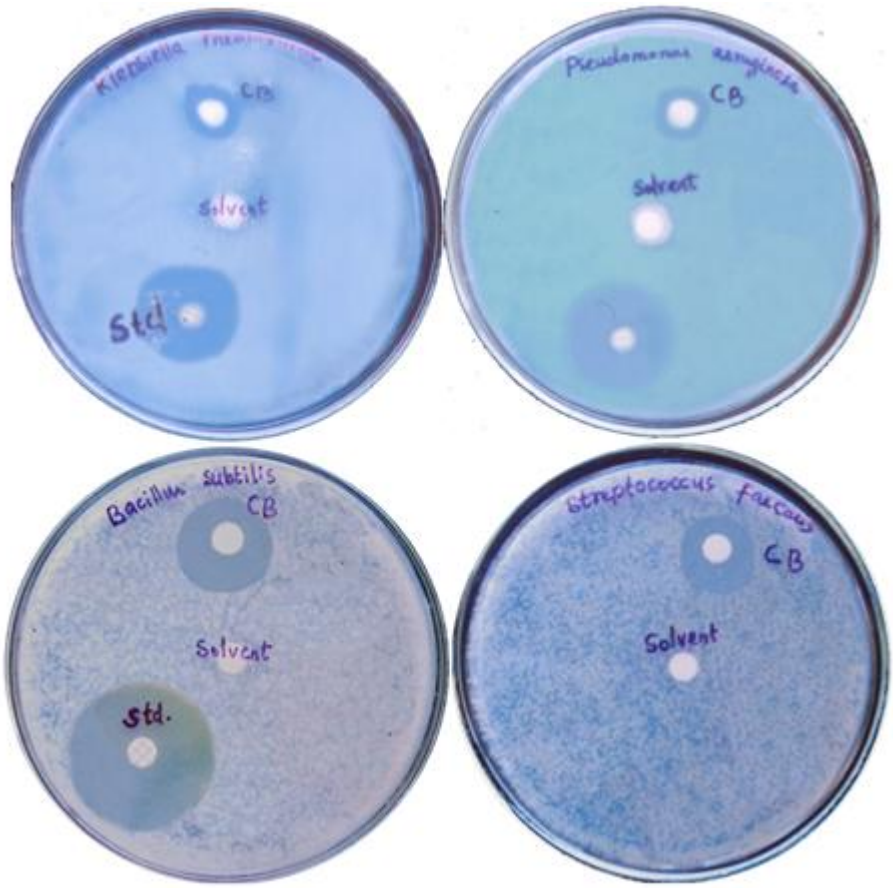

Fig.7.4. Photographs of four culture plates **(a)** *Pseudomonas aeruginosa* **(b)** *Klebsilla pneumoni* **(c)** *Bacillus subtilis* **(d)** *Streptococcus faecaelis*

7.3. Calcium carbonate nanoflakes from waste bond paper

7.3.1. Materials

The bond paper waste used for the synthesis of nanomaterials was collected from printing press.

7.3.2. Synthesis of the materials

About ~12g of crushed bond paper was calcined in a muffle furnace at 600^0 C for four hours. The volatile oxidisable materials were removed under these conditions. The white powdered residue remained after this treatment was taken out and analysed ‘as obtained’. The yield of ‘as obtained’ white ash was recorded to be 5 g (~40%).

7.3.3. Results and discussion

The $CaCO_3$ nanoflakes have been accessed at ~600^0C much lower than its decomposition temperature (~825^0C). The yield of the synthesized materials was found to be around 40% by weight of initial mass. The tap density of the synthesized material was about 1.025 g/cm^3. The as obtained nanoflakes can be readily brought into dispersion by ultrasonication in aqueous and common organic solvent media (ethanol and methanol).

7.3.3.1. Scanning electron microscopy

The morphology of the resulting materials was examined using scanning electron microscopy. The SEM micrographs showed the presence of non uniform agglomerated particles (**Fig.7.5 (a, b)**). The nano particles have a strong tendency to form aggregates due to their high surface energy.

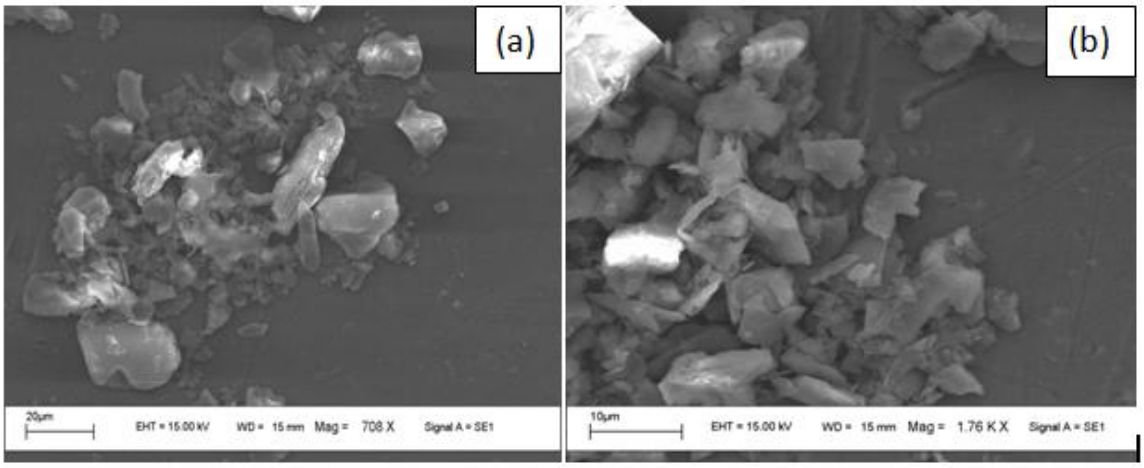

Fig.7.5. (a, b) SEM micrographs of $CaCO_3$ nanoflakes

7.3.3.2. Transmission electron microscopy

The TEM micrographs **(Fig.7.6(a,b))** revealed the presence of nanoflakes. The thicknesses of the flakes are recorded to be ~1.5nm. The high-resolution TEM image revealed highly crystalline nature of the nanoflakes. From HRTEM image **(Fig.7.6(c))** two types of lattice fringes were observed having interplanar distance of 0.384nm and 0.302nm which correspond to (012) and (104) planes of calcite phase of $CaCO_3$ crystal. The SAED) pattern (**Fig.7.6(d)**) showed the concentric rings indicating polycrystalline nature of the material.

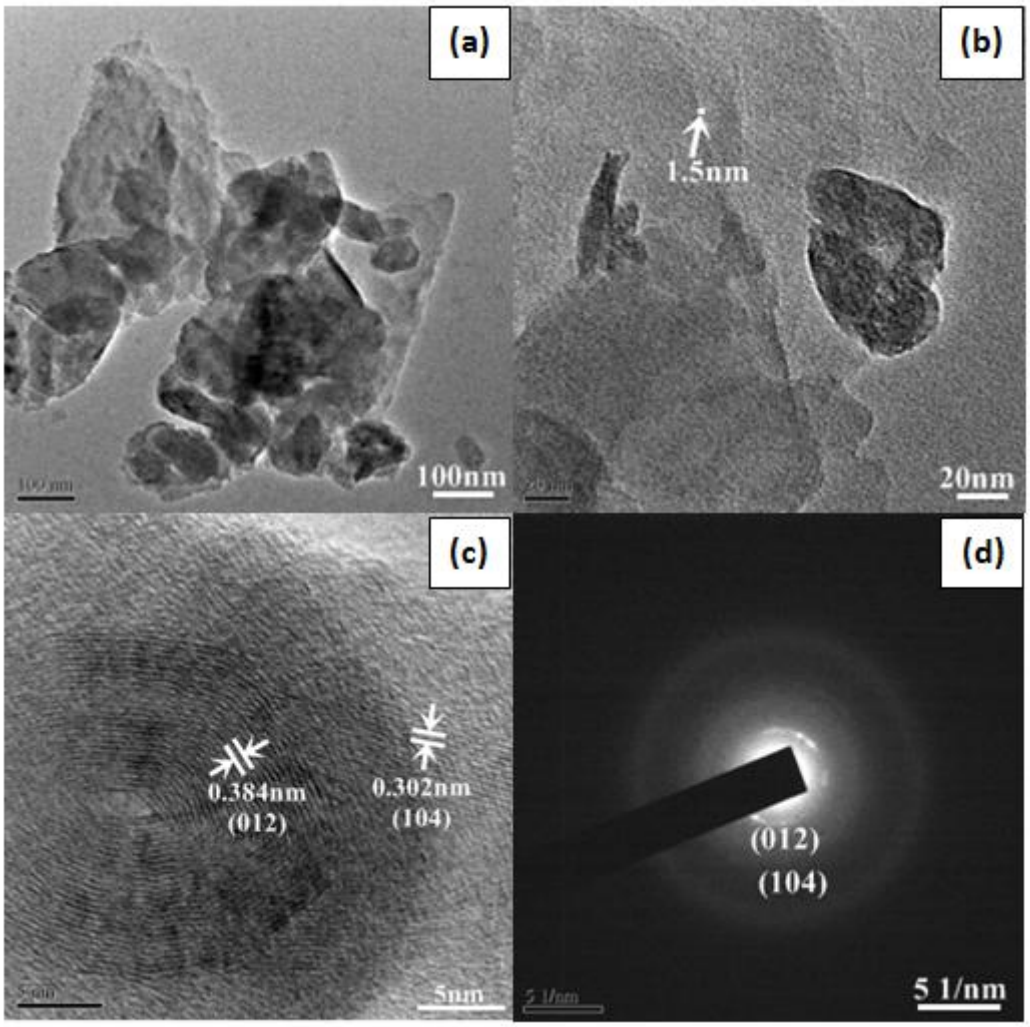

Fig.7.6. (a, b) TEM image **(c)** HRTEM image and **(d)** SAED pattern of $CaCO_3$ nanoflakes.

7.3.3.3. Energy dispersive spectral study

The chemical composition of the synthesized materials was analysed using EDAX **(Fig.7.7)**, which revealed the presence of oxygen, carbon and calcium as the major constituents, along with minor contributions from magnesium, aluminium and silicon.

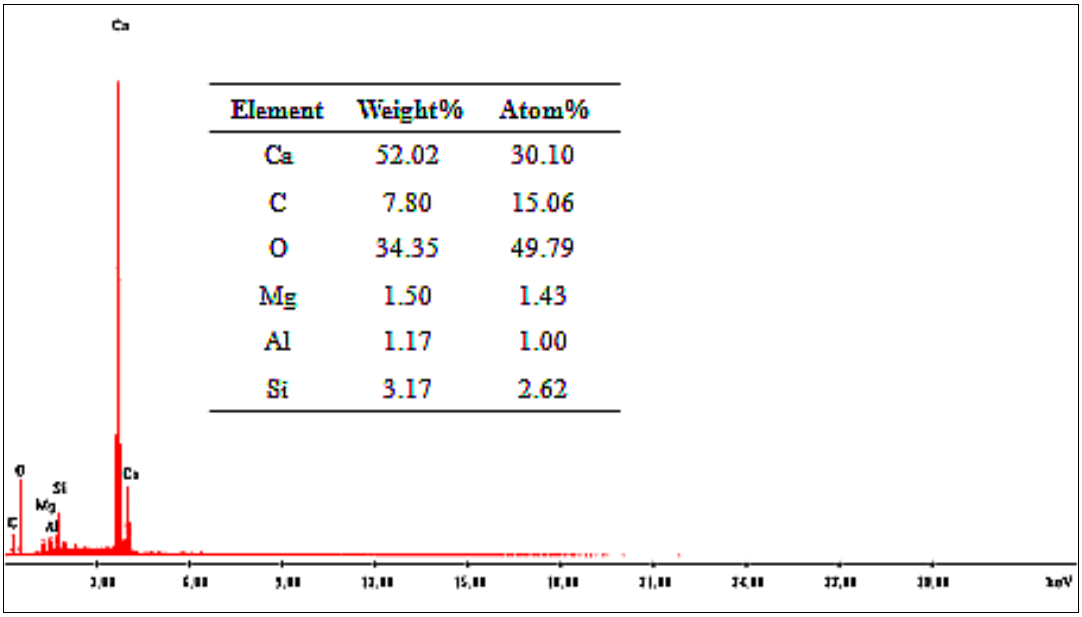

Element	Weight%	Atom%
Ca	52.02	30.10
C	7.80	15.06
O	34.35	49.79
Mg	1.50	1.43
Al	1.17	1.00
Si	3.17	2.62

Fig.7.7. EDAX spectrum and elemental composition of as obtained material

7.3.3.4. FT-IR study

The FT-IR spectrum (**Fig.7.8**) exhibited diagnostic features for the formation of calcite with characteristic absorption bands observed at 712, 872 and 1425 cm^{-1}, corresponding to in-plane bending, out-of-plane bending, and asymmetric stretching modes of CO_3^{2-} absorption bands of calcite. The band at 2505 cm^{-1} is characteristic of C=O stretching of CO_3^{2-} [32-34].

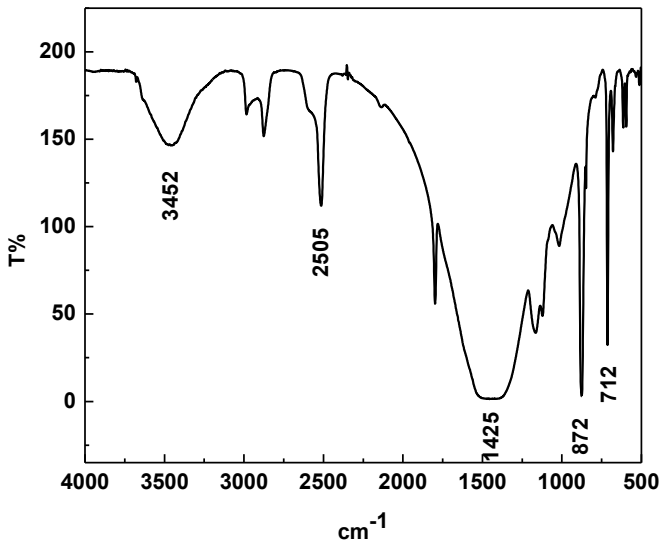

Fig.7.8. FT- IR spectrum of $CaCO_3$ nanoflakes

7.3.3.5. Powder X-ray diffraction study

The X-ray diffraction pattern of the synthesized nanomaterials is shown in **Fig.7.9.** A number of strong Bragg reflections were obtained in the pattern corresponding to the (012), (104), (006), (110), (113), (202), (018), (116), (211), (122), (214), (125), (300), (0012) and (217) reflections of rhombohedral calcite phase of $CaCO_3$ (compared with JCPDS Card No. 85-1108/05-0586) possessing space group $R\bar{3}c$ (137), lattice constant a = 4.980 Å, c = 17.018 Å. All peaks are in good agreement with the calcite structure. The interplanar spacing (d) is calculated using Bragg's Law, $2d\sin\theta = n\lambda$, and is found to be in well agreement with HRTEM data. The average crystallite size and lattice strain are calculated using Debye-Scherrer equation, modified Debye-Scherrer equation and Williamson-Hall equation.

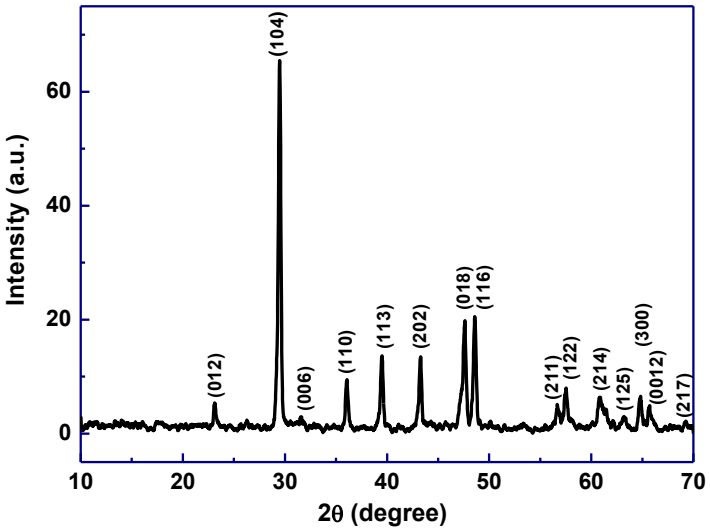

Fig.7.9. XRD pattern of the synthesized nanomaterials

The crystallite size (D) is calculated using the Debye-Scherrer equation, $D = k\lambda/\beta\cos\theta$, that k is the shape factor (0.89), λ is the wavelength of radiation (λ=1.54056 Å), β is full width at half maximum (FWHM) of the particular peak and θ is the Bragg's angle and found to be 28.90 nm for the most intense peak. In calculating the value of β, the contribution from instrumental broadening is taken care of. The evaluated values for each peak are tabulated in **Table7.3.**

Table 7.3 XRD parameter and crystallite size of as obtained material

2θ (degree)	h k l	FWHM (β radian)	Crystallite Size (D nm)	Interplanar Spacing (d nm)
23.12	012	0.00385	36.27	0.384
29.46	104	0.00490	28.90	0.302
31.55	006	0.00953	14.94	0.283
36.00	110	0.00503	28.63	0.249
39.46	113	0.00471	30.90	0.228
43.29	202	0.00463	31.81	0.208
47.58	018	0.00579	25.86	0.190
48.56	116	0.00553	27.17	0.187
56.72	211	0.00631	24.68	0.162
57.53	122	0.00412	37.94	0.160
60.79	214	0.00477	33.27	0.152
63.22	125	0.00954	16.87	0.147
64.83	300	0.00672	24.16	0.143
65.73	0012	0.00905	18.03	0.141
69.25	217	0.00323	51.46	0.135

7.3.3.5.1. Modified Debye-Scherrer equation

Modified Debye-Scherrer equation is derived from Debye-Scherrer equation by taking logarithm of the equation. Debye-Scherrer equation yielded different values of crystallite size for different peaks for the same nanocrystal. However, for a specific nanocrystal, all these peaks should have identical D value for the crystallite size. To get the equal value of D, βcosθ must be identical which is not observed and hence each peak yielded a different value that may be ascribed to the presence of systematic errors on the results. In Modified Scherrer equation, the least square method is used to minimize the errors and to obtain a single value of D through all of the available peaks [35]. Modified Scherrer equation is derived from asic Debye-Scherrer equation as $\beta = k\lambda/D \cos\theta = k\lambda/D. 1/\cos\theta$. Taking logarithm on both sides, the modified Debye-Scherrer equation is obtained as, $\ln\beta = \ln k\lambda/D\cos\theta = \ln k\lambda/D + \ln 1/\cos\theta$. The plot of lnβ against ln 1/cosθ gives a straight line with a slope of around one and an intercept of ln kλ /D. Theoretically this straight line must be with a slope of 45^0

since tan45= 1. Since errors are associated with experimental data, the least squares method is used to obtain the slope and most accurate ln kλ/D. After getting the intercept, the exponential of the intercept is obtained as, $e^{\ln k\lambda/D} = k\lambda/D$. From the intercept of the linear fit, the average crystallite size is calculated and in the present study, it is found to be 26.86 nm.

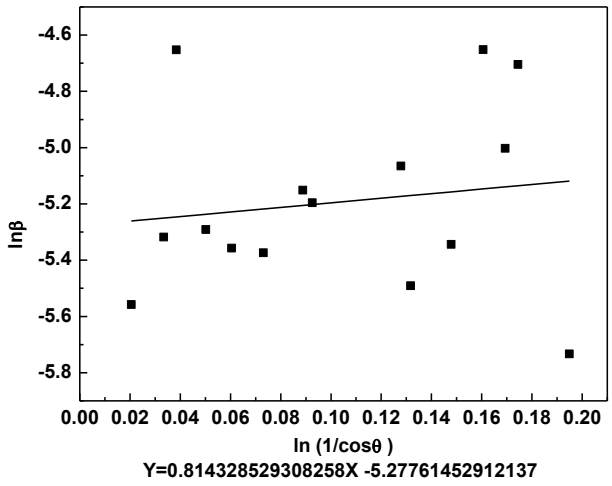

Fig.7.10. Modified Scherrer plot for the synthesized materials

7.3.3.5.2. Williamson-Hall (W-H) approach

In basic Debye-Scherrer equation and also in modified one, the contribution of crystal defect to the broadening of diffraction peak is not considered. In Williamson-Hall approach, the line broadening due to finite size of coherent scattering region and the internal strain are taken into account. In W-H equation, the finite size is taken care of by Debye-Scherrer equation component, k λ /D cos θ and the strain by Wilson component, 4ε tanθ. Thus, in Williamson-Hall equation, $\beta = k\lambda/D\cos\theta + 4\varepsilon\tan\theta$, multiplying both sides by cosθ, the equation takes the linear form as, $\beta\cos\theta = k\lambda/D + 4\varepsilon\sin\theta$. By plotting β cosθ along y- axis and 4sinθ along the x-axis for all peaks, using least square technique, the crystallite size was determined from the slope and the strain from the y-intercept of the fit, respectively (**Fig.7.11**). In the present study, the particle size was evaluated to be 26.8nm and lattice strain to be 8.7×10^{-5}.

The extracted particle size from Williamson Hall plot is in close agreement with that obtained from modified Debye-Scherrer equation. However, the value obtained is lower than that obtained from Debye-Scherrer equation. The crystallite size of the

particles is not generally the same as the particle size due to the presence of polycrystalline aggregates [36, 37].

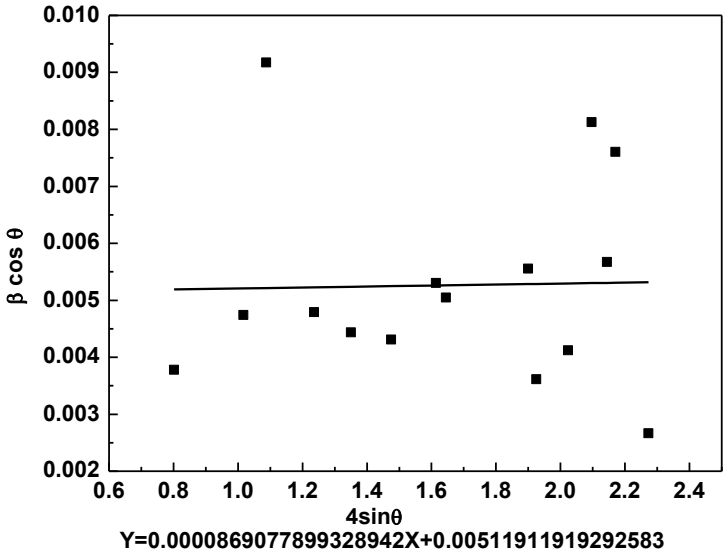

Fig.7.11. Williamson- Hall plot of the calcium carbonate nanoflake

7.3.3.5.3. Specific surface area

Specific surface area(S) is a material property. It has a particular importance in case of adsorption, heterogeneous catalysis and reactions on surfaces. The specific surface area is calculated by Sauter formula, S = 6000/ρ x D, where D is the particle size and ρ is the density [38, 39]. The tap density of the synthesized material is 1.025 g/cm^3 and the average crystallite size is 26.78 nm. Thus the calculated value of specific surface area is 218.58m^2/g.

7.3.3.6. Capacitance Measurement

The two-electrode system is used to evaluate the performance of capacitor cell in 1N KOH electrolyte**.** The Cyclic Voltammograms (CVs) of synthesised material at scan rates of 5 to 500 mV/s exhibited capacitive behaviour with respect to applied voltage of -0.4 to 0.4 V (**Fig.7.12).** CV curve showed a quite rectangular shape at 5 mV/s indicating well developed capacitance properties. Up to the scan rate of 200mV/s, the CV curve showed rectangular shape after that it showed elliptical behaviour. The specific capacitance (Csp) is calculated using the relation, Csp= 1/s x W, where W(g) is the total weight of the material used for construction of cell and s (V/s) is the scan

rate. The specific capacitance of the synthesised material at different scan rate is presented in **Table 7.4.**

Table7.4 Specific capacitance at different scan rate

Scan rate (mV/s)	Current (mA)	Total specific capacitance (F/g)	Specific capacitance of a single electrode (F/g)
5	0.248	24.78	49.56
10	0.428	21.39	42.78
20	0.727	18.19	36.38
50	1.312	13.12	26.24
100	2.430	12.15	24.30
200	3.996	9.99	19.98
500	7.481	7.48	14.96

It is observed from **Table7.4**, that scan rate is inversely proportional to specific capacitance. As the scan rate increases, current increases but specific capacitance decreases **(Fig.7.12).** It is considered that slowing down the scan rate can allow electrolyte to penetrate into pores more thoroughly and to make greater contact with the internal surface of the electrode material and hence more charge is stored on the surface of electrode and yield a larger measured capacitance that is closer to the intrinsic capacitance. At higher scan rate electrolyte get less time to contact with the complete electrode surface and less charge stored on electrode surface which results into low capacitance [40, 41].

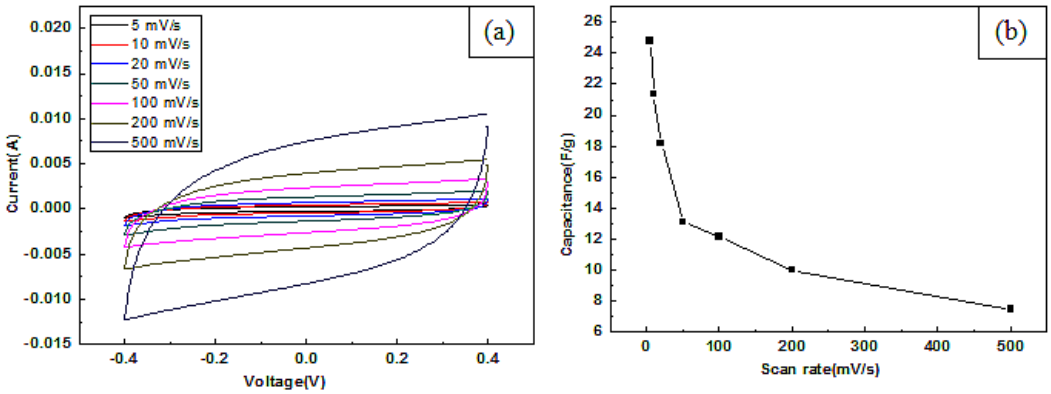

Fig.7.12. (a) CV curve of the synthesised material at different scan rate (5 - 500 mV/s) in 1N KOH solution and **(b)** effect of scan rate on capacitance

7.4. Calcium carbonate nanoparticles from leaves of *Dalbergia sissoo*

7.4.1. Materials

The raw materials used for the synthesis were matured leaves of *Dalbergia sissoo* (**Fig.7.13**), collected from S. S. College premises, Hailakandi, Assam, India. The biomass was thoroughly washed, sun dried and used as precursor to synthesize nanoparticles.

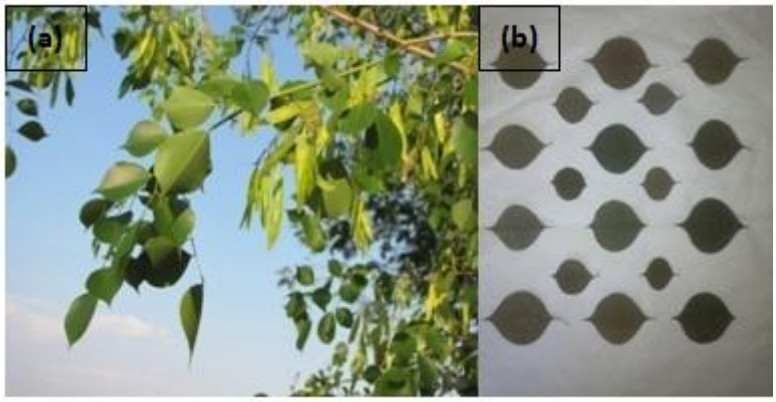

Fig.7.13. (a, b) Photographs of leaves of *Dalbergia sissoo*

7.4.2. Synthesis of the nanoparticles

A few dried leaves of *Dalbergia sissoo* (approx. 10 g), finely crushed into powder were taken in a quartz boat and calcined in muffle furnace at 500^0C for one and half an hours. The volatile oxidisable materials were removed under these conditions. The white powdered residue remained after this treatment was taken out and analysed 'as obtained'. The yield was recorded to be 1.2g.

7.4.3. Results and discussion

The synthesized nanoparticles were white and found to be stable in air for months. The yield was recorded to be around 12% by weight of initial mass. The tap density of the synthesized nanoparticles was about 0.447 g/cm^3.

7.4.3.1. Scanning electron microscopy

The morphology of the resulting materials was examined using scanning electron microscopy. The SEM micrograph (**Fig.7.14 (a, b)**) exhibited the presence of non uniform agglomerated porous particles.

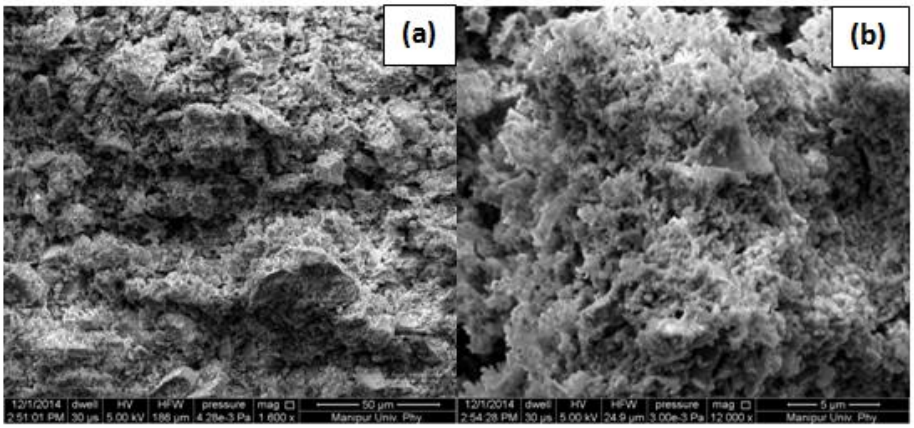

Fig.7.14. (a, b) SEM micrographs of the synthesised materials

7.4.3.2. Transmission electron microscopy

The TEM micrographs **(Fig.7.15)** exhibited the presence of non uniform agglomerated nanoparticles of size ~90 nm. The nanoparticles have a strong tendency to form aggregates due to their high surface energy. The high-resolution TEM image **(Fig.7.15 (c))** revealed highly crystalline nature of the nanoparticles and the lattice fringes were observed to be at interplanar distance of 0.384nm which correspond to (012) plane of calcite phase of $CaCO_3$ crystal. The electron diffraction (ED) pattern showed systematic pattern of spots indicating single crystalline nature of the material.

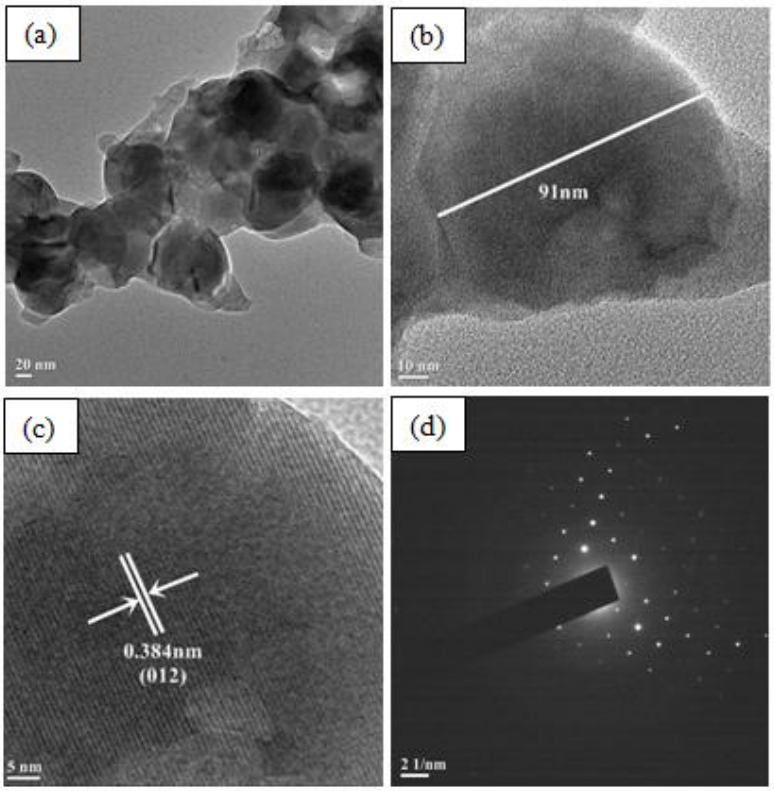

Fig.7.15 (a, b) TEM image **(c)** HRTEM image and **(d)** ED pattern of nanomaterial

7.4.3.3. Energy dispersive spectral study

The elemental compositions of the synthesized materials were analysed using EDAX. The study revealed **(Fig.7.16)** the presence of calcium, carbon and oxygen as the major constituents, along with minor contributions from magnesium, aluminium, silicon, molybdenum, chlorine and potassium. This analysis showed that the composition of the calcium carbonate in the synthesized material is not pure due to the presence of trace of other elements.

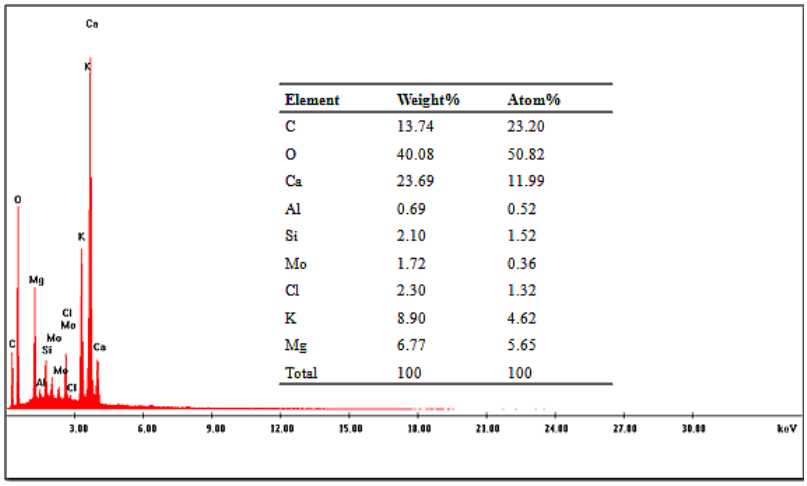

Element	Weight%	Atom%
C	13.74	23.20
O	40.08	50.82
Ca	23.69	11.99
Al	0.69	0.52
Si	2.10	1.52
Mo	1.72	0.36
Cl	2.30	1.32
K	8.90	4.62
Mg	6.77	5.65
Total	100	100

Fig.7.16. EDAX spectrum and elemental composition of as obtained materials

7.4.3.4. X-Ray diffraction study

The powder X-ray diffraction pattern was recorded for identification of phases exhibited by the synthesised material. The X-ray diffraction pattern **(Fig.7.17)** of the nanoparticles showed diffraction peaks which were indexed to be typical calcite rhombohedral $CaCO_3$ (space group space group $R\bar{3}c$(137), JCPDS file No.85-1108/24-0027) and no extra peaks of other phases were observed.

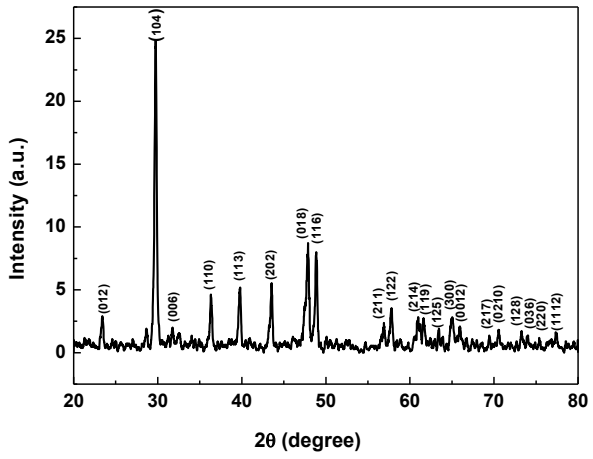

Fig.7.17. XRD pattern of nanomaterials from leaves of *Dalbergia sissoo*

The interplanar spacing (d), for the most intense peak was calculated using Bragg's law and found to be 0.30 nm. The average crystallite size estimated by the Debye-Scherrer formula, using a Gaussian fit was found to be about 26. 4 nm. The calculated values for each peak are tabulated in **Table 7.5.**

Table7.5 XRD parameter and crystallite size (D) of the synthesized material

2θ (degree)	**h k l**	**Interplanar spacing (d nm)**	**FWHM (β radian)**	**Crystallite size (D nm)**
23.39	012	0.380	0.00608	23.03
29.75	104	0.300	0.00538	26.39
31.76	006	0.283	0.00525	27.14
36.34	110	0.247	0.00466	30.99
39.75	113	0.226	0.00561	25.97
43.51	202	0.207	0.0058	25.45
47.83	018	0.189	0.00684	21.93
48.85	116	0.186	0.00466	32.30
56.89	211	0.161	0.00472	32.98
57.77	122	0.159	0.00607	25.80
60.97	214	0.151	0.00605	26.28
61.63	119	0.150	0.00543	29.39
63.42	125	0.146	0.00355	45.36
65.00	300	0.143	0.01006	16.16
65.93	0012	0.141	0.00447	36.53
69.45	217	0.135	0.00396	42.10
70.55	0210	0.133	0.00486	34.59
73.30	128	0.129	0.00584	29.26
73.99	036	0.128	0.00535	32.08
75.50	220	0.125	0.00226	76.78
77.39	1112	0.123	0.00496	35.40

7.4.3.4.1. Modified Debye-Scherrer equation

The Scherrer equation gives a rough estimate of particle size. Despite the well-known accuracy of this method, it does not give a single value of D for each peak. It neglects the importance of the micro strain, ε, and its effects in the powder diffraction pattern. Considering the presence of systematic error on the results obtained from each peak, a modified Scherrer formula is used to obtain a better average value of D, least square method is used to mathematically decrease the source of errors **(Fig.7.18)** [35]. The average crystallite size is calculated to be 22.76 nm. The value obtained from modified Scherrer equation is lower than the average value discussed earlier.

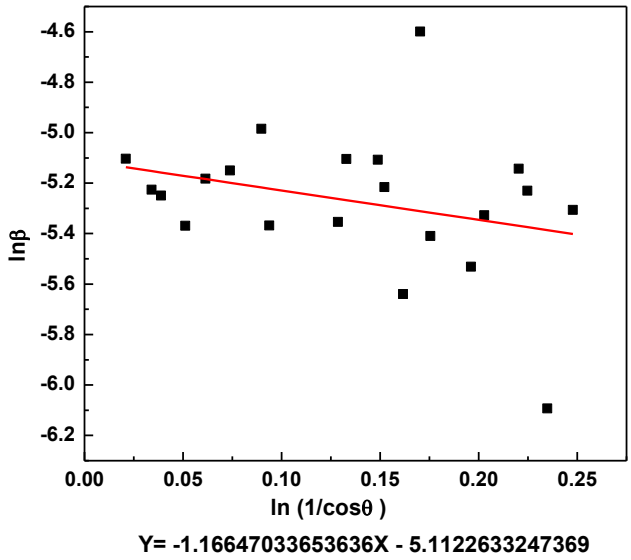

Fig.7.18. Modified Scherrer plot for the synthesized materials

7.4.3.4.2. Williamson-Hall (W-H) approach

The Modified Scherrer equation gives a better estimation of single valued average crystallite size; however, it is silent about the importance of the micro strain, ε, and its effects in peak broadening of the powder diffraction pattern. Further, the crystallite size depends on the peak broadening of the diffracted peaks. Williamson-Hall analysis is a simplified integral breadth method where both size-induced and strain-induced broadening is deconvoluted by considering the peak width as a function of 2θ [36]. The Williamson-Hall plot of the synthesised sample is obtained by putting $\beta\cos\theta$ along vertical axis and $4\sin\theta$ along the horizontal axis, for all peaks from 2θ = 20º to 2θ =80º. From the least square fit, one can estimate the strain from the slope of the fitted line and crystallite size (D) from its intersection with the y-axis (**Fig.7.19**). The

extracted particle size is 20.63nm and lattice strain is -1.05945589735647x 10^{-3}. The negative slope of the fitted line in a Williamson-Hall plot indicates the presence of a compressive strain in the crystal lattice of the sample. The negative strain indicates the piezoelectric potentiality of the material [36, 37].

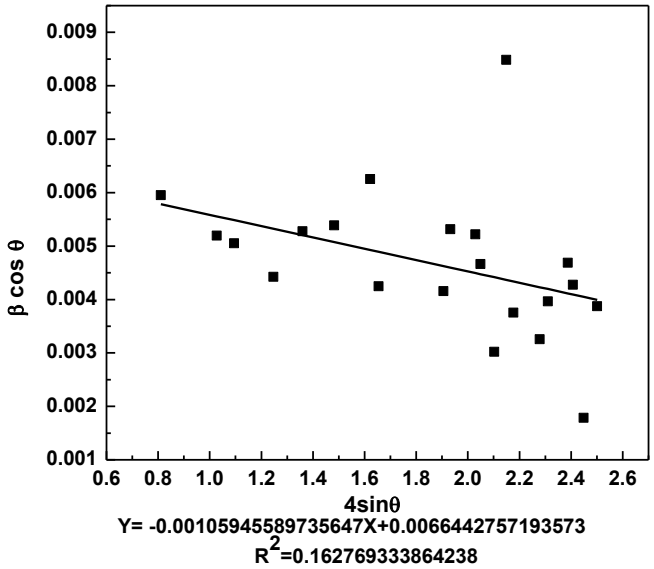

Fig.7.19 Williamson-Hall plot of the synthesised material

The value of crystallite size calculated by Debye -Scherrer method is higher than that obtained by both modified Debye-Scherrer method and Williamson-Hall method. However, the modified Debye -Scherrer method and Williamson-Hall method is showing close agreement in the result.

Specific surface area (SSA) calculated by Sauter formula was found to be 650.65m^2/g. The surface area of the synthesized material is found to be very large which indicates its potentiality in heterogeneous catalysis.

7.4.3.5. Photocatalytic activity

Environmental problems such as toxic organic pollutants provide the impetus for fundamental and applied research into environmental areas. Semiconductor photocatalysts have attracted considerable attention for a long time in the fields of photochemistry [42-46] because of their usefulness with regard to solving environmental problems. Over the last few years, considerable efforts have been made in the controlled synthesis of various nanosized materials to improve their properties

for photo-catalysis. Porous materials have been the subject of intensive research because of their potential applications in optoelectronics, biotechnology, pharmaceutics, catalysis, etc. The photocatalytic activity of the as obtained material was evaluated by degradation of methylene blue (MB) solution under visible light irradiation. The decreasing concentration of the MB solution in the photocatalytic reaction was used to determine the effectiveness of the material as catalyst [47, 48].

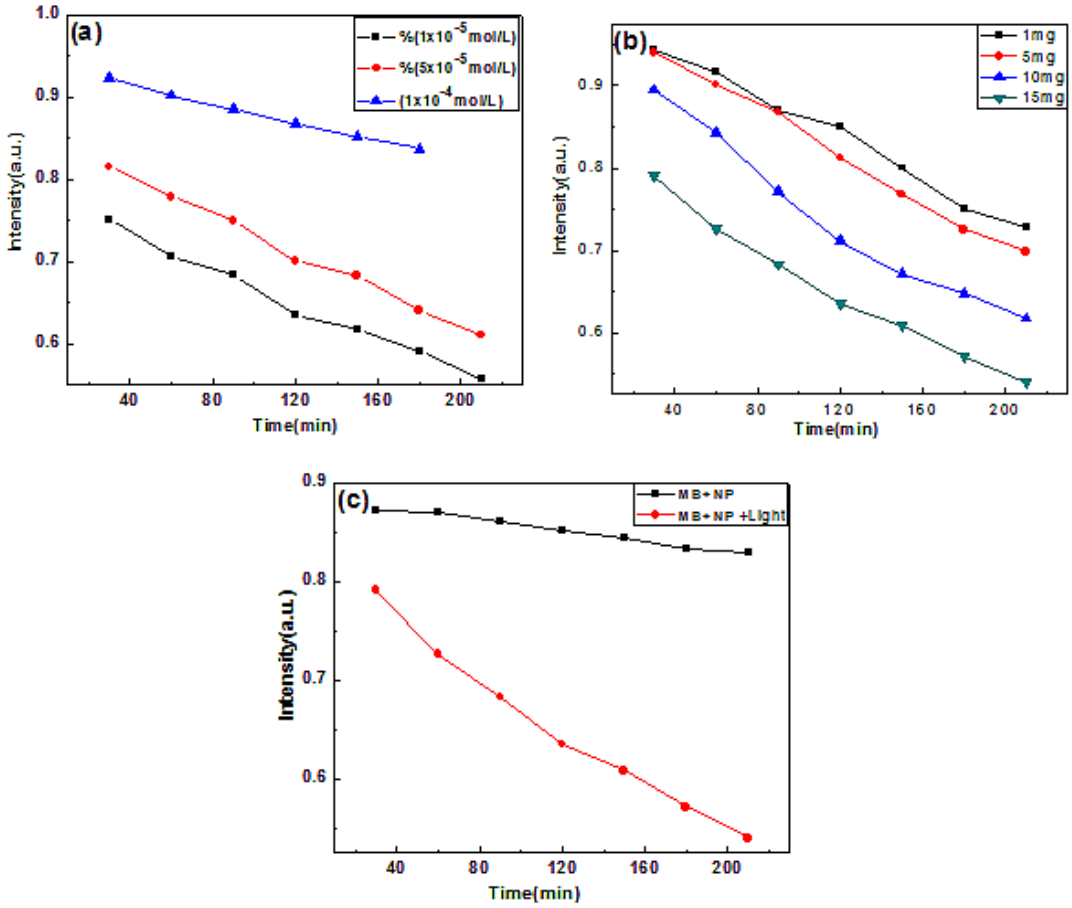

Fig.7.20 (a) Time dependent UV-visible peak intensities at 665 nm of different concentrations of MB solution **(b)** concentration dependent UV-visible intensities at 665nm of ($1x10^{-5}$ mol/L) with different amounts of nanoparticles and **(c)** degradation of MB solution ($1x10^{-5}$ mol/L) with visible light treated product (MB+NP+ Light) and non treated product (MB+NP).

The intensity of the 665 nm peak of MB solution was monitored to assess the concentration of the MB in solution. 1mg, 5mg, 10mg and 15mg of as-obtained nanoparticle as photocatalyst were added into 50mL of MB solution in distilled water of concentrations $1x10^{-5}$ mol/L, $5x10^{-5}$mol/L and $1x10^{-4}$mol/L, respectively. After

being dispersed in an ultrasonic bath for 5min, the solutions were stirred for 2 hour in the dark to reach adsorption equilibrium between the catalyst and the solution and then exposed to visible-light irradiation. The samples are taken out at specific time interval and centrifuged to separate any suspended particle. The readings are taken in a spectrophotometer at an interval of 30, 60, 90, 120, 150, 180 and 210 minutes. It is observed that nanoparticles alone as such do not exhibit any degradation behaviour in absence of light but degradation **(Fig.7.20)** occurs remarkably on exposure to visible light.

7.5. Quasi-spherical calcium carbonate nanoparticles from leaves of *Delonix regia*

7.5.1. Materials

The leaves of *Delonix regia* (**Fig.7.21**), a tropical ornamental plant were collected from the plains of North Eastern region of India during May and June 2012. The leaves were thoroughly washed, sun dried, crushed and used as precursor to synthesize nanoparticles. Locally known as krishnachura or gulmohar, this plant belongs to Caesalpiniaceae family. It serves as useful shade tree in tropical climatic conditions.

Fig.7.21. Photograph of leaves of *Delonix regia*

7.5.2. Synthesis of the nanoparticles

A few dried leaves of *Delonix regia* (approx. 10 g), finely crushed into powder was taken in a quartz boat and calcined in muffle furnace at 500^0C for 1½ hour. The volatile oxidisable materials were removed under these conditions. The white powdered residue remained after this treatment was taken out and analysed. The yield recorded was 0.7g.

7.5.3. Results and discussion

The synthesized nanoparticles were white and found to be stable in air for months. The yield was recorded to be around 7% by weight of initial mass. The tap density of the synthesized materials was found to be about 0.463 g/cm^3.

7.5.3.1. Transmission electron microscopy

The TEM micrographs (**Fig.7.22 (a, b)**) of the as-obtained material showed the presence of quasi-spherical particles of size around 20- 40nm. The high-resolution TEM image revealed highly crystalline nature of the material. The lattice fringes between two adjacent planes are 0.384nm apart, which resembles the interplanar distance of (012) plane of calcite phase of $CaCO_3$ crystal **(Fig.7.22(c)).** The SAED showed systematic pattern of spots indicating single crystalline nature of the material.

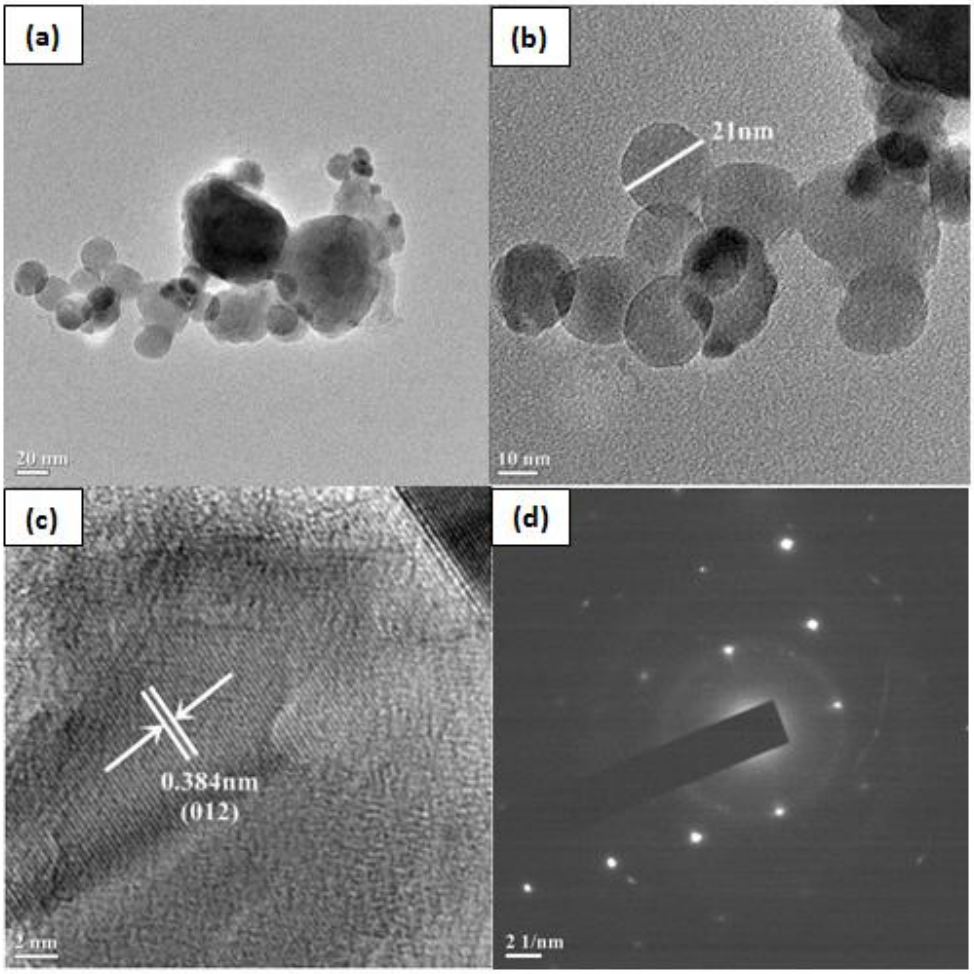

Fig.7.22. (a, b) TEM images **(c)** HRTEM image and **(d)** SAED pattern of the materials obtained from the leaves of *Delonix regia*

7.5.3.2. Powder X-ray diffraction study

The X-ray diffraction pattern **(Fig.7.23)** of the synthesized nanomaterials showed a number of strong Bragg reflections which may be indexed as (012), (104), (006), (110), (113), (202), (018), (116), (211), (122), (214), (125), (300), (0012) and (217) reflections of calcite rhombohedral calcium carbonate (compared with JCPDS Card No85-1108/05-0586) possessing space group $R\bar{3}c$ (137), lattice constant a = 4.980 Å, c = 17.018 Å. All peaks are very well matched with the calcite structure. The Bragg reflection obtained in the pattern corresponding to (011) plane resembles hexagonal SiO_2 ((JCPDS file no.85-0504). The inter planar spacing (d=0.384 nm) calculated using Bragg's equation is found to be in well agreement with HRTEM data. The average crystallite size estimated by the Debye-Scherrer equation using a Gaussian fit was found to be ~40 nm which is compatible with that obtained from TEM study.

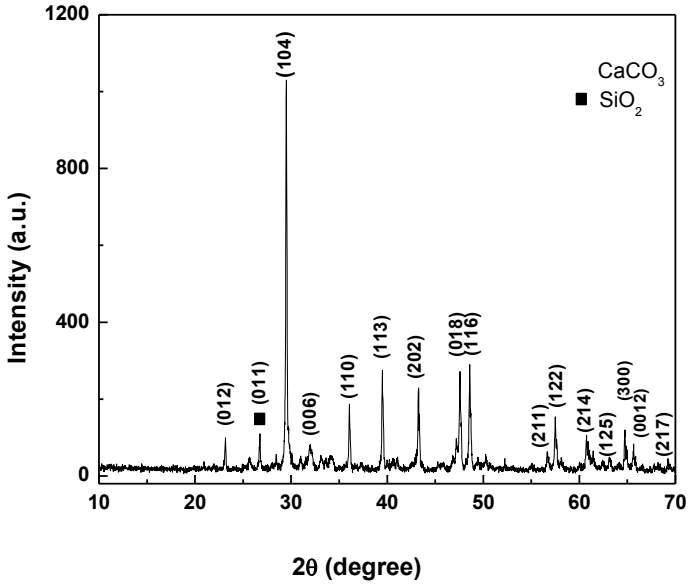

Fig.7.23.XRD pattern of the material obtained from leaves of *Delonix regia*

References

[1] Duan, S., & Wang, R. *Prog. Nat. Sci. Mater.*, 2013, **23**, 113.

[2] Chaturvedi, S., Dave, P. N., & Shah, N. K. *J. Saudi. Chem. Soc.*, 2012, **16**, 307.

[3] Kumar, R. A., Sivashanmugam, A., Deepthi, S., Bumgardner, J. D., Nair, S. V., & Jayakumar, R. *Carbohydr. Polym.*, 2016, **140**, 144.

[4] Reddy, N. S., Sowmya, S., Bumgardner, J. D., Chennazhi, K. P., Biswas, R., & Jayakumar, R. *Biochim. Biophys. Acta*, 2014, **1840**, 2080.

[5] Osterwalder, N., Loher, S., Grass, R. N., Brunner, T. J., Limbach, L. K., Halim, S. C., & Stark, W. J. *J. Nanopart. Res.*, 2007, **9**, 275.

[6] Sunqing, Q., Junxiu, D., & Guoxu, C. *Lubr. Sci*., 2000, **12**, 205.

[7] Boyjoo, Y., Pareek, V. K., & Liu, J. *J. Mater. Chem. A*, 2014, **2**, 14270.

[8] Tang, J., Sun, D. M., Qian, W. Y., Zhu, R. R., Sun, X. Y., Wang, W. R., & Wang, S. L. *Biol. Trace Elem. Res.*, 2012, **147**, 408.

[9] Tsuzuki, T., Pethick, K., & McCormick, P. G. *J. Nanopart. Res.*, 2000, **2**, 375.

[10] Atchudan, R., Na, H. B., Cheong, I. W., & Joo, J. *J. Nanosci. Nanotechnol*., 2015, **15**, 2702.

[11] Huber, M., Stark, W. J., Loher, S., Maciejewski, M., Krumeich, F., & Baiker, A. *Chem. Commun.*, 2005, **5**, 648.

[12] Chen, J. F., Ding, H. M., Wang, J. X., & Shao, L. *Biomaterials*, 2004, **25**, 723.

[13] Shan, D., Zhu, M., Xue, H., & Cosnier, S. *Biosens. Bioelectron.*, 2007, **22**, 1612.

[14] Halozan, D., Riebentanz, U., Brumen, M., & Donath, E. *Colloids Surf. A*, 2009, **342**, 115.

[15] Koivula, H., Toivakka, M., & Gane, P. *J. colloid interface sci.*, 2012, **369**, 426.

[16] Viravaidya, C., Li, M., & Mann, S. *Chem. Commun.*, 2004, **19**, 2182.

[17] Thomas, M. V., & Puleo, D. A. *J. Biomed. Mater. Res. B Appl. Biomater.*, 2009, **88**, 597.

[18] Peltier, L. F., Bickel, E. Y., Lillo, R., & Thein, M. S. *Ann. Surg.*, 1957, **146**, 61.

[19] Le Geros, R. Z. *Chem. Rev.*, 2008, **108**, 4742.

[20] Santschi, E. M., & Mc Garvey, L. *Vet. Surg.*, 2003, **32**, 128.

[21] Stabile, D. E., & Jacobs, A. M. *J. Am. Podiatr. Med. Assoc.*, 1990, **80**, 354.

[22] Gitelis, S., & Brebach, G. T. *J. Orthop. Surg.*, 2002, **10**. 53.

[23] Liu, R., Zou, H., Guo, F., Chen, J., Zhao, Y., & Gao, L. *Chinese J. Mater. Res*., 2001, **1**, 61.

[24] Shen, Q., Wei, H., Wang, L., Zhou, Y., Zhao, Y., Zhang, Z., & Xu, D. *J. Phys. Chem. B*, 2005, **109**, 18342.

[25] Sukhorukov, G. B., Volodkin, D. V., Gunther, A. M., Petrov, A. I., Shenoy, D. B., & Möhwald, H. *J. Mater. Chem.*, 2004, **14**, 2073.

[26] Misra, M. K., Ragland, K. W., & Baker, A. J. *Biom. Bioen.*, 1993, **4**, 103.

[27] Farrugia, L. J. *J. Appl. Crystallogr.*, 1999, **32**, 837.

[28] CIF files. File number: 5000040; Available online: http://cod.ibt.lt

[29] Cheng, G. C. H., & Zussman, J. *Acta Crystallogr.*, 1963, **16**, 767.

[30] Mercury 1.4.1 ®. Available online: http://www.ccdc.cam.ac.uk

[31] Heinlaan, M., Ivask, A., Blinova, I., Dubourguier, H. C., & Kahru, A. *Chemosphere*, 2008, **71**, 1308.

[32] Ghadami J.l G. A., & Idrees, M. *Iran. J. Chem. Chem. Eng.*, 2013, **32**, 27.

[33] Islam, K. N., Zuki, A. B. Z., Ali, M. E., Hussein, M. Z. B., Noordin, M. M., Loqman, M. Y., & Hamid, S. B. A. *J. Nanomater.*, 2012, **2**, 1.

[34] Vagenas, N. V., Gatsouli, A., & Kontoyannis, C. G. *Talanta*, 2003, **59**, 831.

[35] Monshi, A., Foroughi, M. R., & Monshi, M. R. *World J. Nano Sci. Eng.*, 2012, **2**, 154.

[36] Prabhu, Y. T., Rao, K. V., Kumar, V. S. S., & Kumari, B. S. *Int. J. Eng. Adv. Technol.*, 2013, **2**, 2249.

[37] Mote, V. D., Purushotham, Y., & Dole, B. N. *J. Theor. Appl. Phys.*, 2012, **6**, 1.

[38] Schuler, T., & Tremel, W. Chem. Commun. 2011, **47**, 5208.

[39] Theivasanthi, T., & Alagar, M. Nano Biomed Eng 2012;4:58-6

[40] Largeot, C., Portet, C., Chmiola, J., Taberna, P. L., Gogotsi, Y., & Simon, P. *J. Am. Chem. Soc.*, 2008, **130**, 2730.

[41] Amitha, F. E., Reddy, A. L. M., & Ramaprabhu, S. *J. Nanopart. Res.*, 2009, **11**, 725.

[42] Nosaka, Y., Matsushita, M., Nishino, J., & Nosaka, A. Y. *Sci. Technol. Adv. Mater.*, 2005, **6**, 143.

[43] Cao, F., Shi, W., Zhao, L., Song, S., Yang, J., Lei, Y., & Zhang, H. *J. Phys. Chem. C*, 2008, **112**, 17095.

[44] Ni, Y., Zhang, L., Zhang, L., & Wei, X. *Cryst. Res. Technol.*, 2008, **43**, 1030.

[45] Wu, H. Q., Wang, Q., Yao, Y. Z., Qian, C., Cao, P. P., Zhang, X. J., & Wei, X. W. *Mater. Chem. Phys.*, 2009, **113**, 539.

[46] Xiong, S., Xi, B., Wang, C., Xi, G., Liu, X., & Qian, Y. *Chem. Eur. J.*, 2007, **13**, 7926.

[47] Chang, T., Li, Z., Yun, G., Jia, Y., & Yang, H. *Nano-Micro Lett.*, 2013, **5**, 163.

[48] Woan, K., Pyrgiotakis, G., & Sigmund, W. *Adv. Mater.*, 2009, **21**, 2233.